Theory of terahertz/near-infrared optical mixing in quantum wells in strong magnetic fields

Takeshi Inoshita, Junichiro Kono,* and Hiroyuki Sakaki
Quantum Transition Project, JST, 4-7-6-4F Komaba, Meguro-ku, Tokyo 153, Japan
and RCAST, University of Tokyo, 4-6-1 Komaba, Meguro-ku, Tokyo 153, Japan
(Received 14 October 1997)

Recently, strong near-band-gap emission lines, or sidebands, were discovered in undoped GaAs quantum wells illuminated simultaneously by near-infrared and terahertz (THz) radiation in strong magnetic fields [J. Kono *et al.*, Phys. Rev. Lett. **79**, 1758 (1997) and references therein]. We have developed a perturbation theory for this phenomenon. Assuming that the THz radiation induces transitions between magnetoexciton levels, we modeled the sideband generation as a third-order optical process and obtained the susceptibility. Our theory successfully explains all the observed features of the sidebands. Moreover, we have shown that the magnetic-field dependence of the sideband intensities exhibits a rich spectrum of resonances that originate from intraexciton transitions, demonstrating the power and usefulness of sideband generation in relation to magnetoexciton spectroscopy. [S0163-1829(98)08708-6]

I. INTRODUCTION

Electromagnetic radiation in the THz regime (0.1–10 THz) is unique in that it lies between photons and ac electric fields, sharing the characteristics of both. Moreover, it covers the important energy range of intersubband transitions in quantum-confined semiconductor structures, which is extremely important for infrared detector/emitter applications. Despite these interests, however, the interaction of strong THz radiation with matter has long remained unexplored, at least experimentally, due to the lack of a tunable coherent source of THz radiation. The advent of free-electron lasers[1] that are continuously tunable in the THz range filled this gap and aroused keen interest in the THz physics of condensed matter, in particular, mesoscopic semiconductor structures. Striking discoveries have already been reported concerning the transport[2–8] as well as optical properties of such THz-driven systems.[9–15]

The present paper concerns the resonant THz sideband generation discovered recently in undoped GaAs/$Al_xGa_{1-x}As$ multiple quantum wells (MQW's).[11–15] In these experiments, when the sample is illuminated simultaneously by THz (frequency ω_T) and near-infrared (frequency ω_N) radiation, strong and sharp sidebands with frequencies $\omega_N \pm 2\omega_T$ are observed. (Higher-order sidebands with frequencies $\omega_N \pm 4\omega_T$ are also observed, but we will not consider them in the present paper.) The experimental findings can be summarized as follows: (1) The sidebands are observable only when ω_N is tuned to an interband [e.g., $1s$ heavy-hole (HH)] exciton absorption peak. No sidebands are observed when ω_N is below the band gap or between two exciton absorption peaks (e.g., $\omega_{1s} < \omega_N < \omega_{2s}$). (2) When ω_N is tuned to the lowest ($1s$) HH exciton peak (ω_{1s}), the lower ($\omega_N - 2\omega_T$) sideband is absent, and only the upper ($\omega_N + 2\omega_T$) sideband is observed. If ω_N is tuned to higher ($2s$ or $3s$) exciton peaks, both the upper and lower sidebands are observable. (3) The sideband intensities I exhibit pronounced resonances as functions of magnetic field B. (4) I is maximum (minimum) for linearly (circularly) polarized THz radiation.

These experiments were mostly done in the regime $I \propto I_T^2 I_N$, where I_T and I_N are the intensities of the THz and near-infrared (NIR) radiation, respectively. This suggests that the sideband generation can be described as a third-order nonlinear optical process.

In this paper, we present a perturbation theory for the THz sideband generation based on a magnetoexciton model. It will be shown that the theory gives a semiquantitative explanation to all the experimental findings mentioned above. Furthermore, we will demonstrate that the resonances in the I-B curve provide valuable information on the s-p and s-s intraexciton transition energies, rendering sideband generation a new class of magnetoexciton spectroscopy.

The outline of our paper is as follows. Section II is devoted to the formalism and general conclusions drawn from it. In Sec. II A, we define the perturbation processes responsible for the sideband generation. It is followed by Sec. II B where we discuss our magnetoexciton model and describe how its eigenstates are calculated. This section is rather sketchy, more details being given in Appendixes A and B. The results of these two subsections are combined in Sec. II C to obtain the expression for the third-order susceptibility χ. This expression is then analyzed in terms of resonances (Sec. II D) and polarization dependence (Sec. II E). The results of numerical calculations are presented and compared with experiment in Sec. III (and also in Appendix C). A summary of conclusions is given in Sec. IV. Throughout the paper we will use the unit $\hbar = 1$.

II. FORMULATION AND GENERAL CONSIDERATIONS

A. Perturbation processes

We consider a nondope MQW placed in a perpendicular magnetic field and calculate third-order optical susceptibility tensors χ for the sidebands defined by[16]

$$P_i^{(+)}(\omega_N + 2\omega_T) = \sum_{jkl} \chi_{ijkl} E_j^{(+)}(\omega_T) E_k^{(+)}(\omega_T) E_l^{(+)}(\omega_N) \quad \text{(upper sideband)}, \tag{1a}$$

$$P_i^{(+)}(\omega_N-2\omega_T)=\sum_{jkl}\chi_{ijkl}E_j^{(-)}(\omega_T)E_k^{(-)}(\omega_T)E_l^{(+)}(\omega_N)$$

$$\text{(lower sideband)}, \tag{1b}$$

where i,j,k,l denote the in-layer Cartesian coordinates x and y, and $\boldsymbol{P}^{(+)}(\omega)$ is defined through the Fourier expansion of the polarization: $\boldsymbol{P}(t)=\Sigma_m\{\boldsymbol{P}^{(+)}(\omega_m)\exp(-i\omega_m t)+\boldsymbol{P}^{(-)}(\omega_m)\exp(i\omega_m t)\}$ $(\omega_m>0)$. Namely, $\boldsymbol{P}^{(\pm)}(\omega)$ are the positive $(+)$ and negative $(-)$ frequency components. To ensure that $\boldsymbol{P}(t)$ is real, $\boldsymbol{P}^{(+)}(\omega)=[\boldsymbol{P}^{(-)}(\omega)]^*$ must be satisfied. A similar decomposition is carried out for the electric field $\boldsymbol{E}(t)$ as well. We assume that the propagation directions of the THz and NIR beams (plane waves) are normal to the MQW. Because of this and because the wavelengths of the beams are much larger than the well width, we can neglect the coordinate dependence of $\boldsymbol{P}(t)$ and $\boldsymbol{E}(t)$.

Let us study the time evolution of the electrons in a well. At zero temperature and in a strong magnetic field, the system is initially in its ground state $|g\rangle$ with all the valence-band Landau levels (LL's) filled and all the conduction-band LL's empty. In the electron-hole picture, this is the vacuum state with no electron or hole. We can safely assume that the NIR and THz beams induce only interband and intraband transitions, respectively. Then, the THz radiation cannot perturb this ground state. The first possible transition is a NIR photon absorption that produces an s exciton. This exciton is excited to a p state by absorbing a THz photon, then into an s state by absorbing another THz photon, and finally recombines to produce an up-converted $(\omega_N+2\omega_T)$ photon. (The first and the second s states may or may not be the same.) This gives rise to the upper sideband. The corresponding Feynman diagrams for the density matrix are illustrated in Figs. 1(a) and 1(b). On the other hand, if the two THz photons are *emitted* (stimulated emission) rather than absorbed as shown in Figs. 1(a′) and 1(b′), we have lower sideband generation $(\omega_N-2\omega_T)$.

The expectation value of the polarization can be expressed, using the density operator ρ, as

$$\boldsymbol{P}=\mathrm{tr}(-e\rho\boldsymbol{r})=\frac{-ie}{m_0}\sum_{a,b}\frac{\rho_{ab}\boldsymbol{\pi}_{ba}}{\omega_{ab}}, \tag{2}$$

where $\omega_{ij}=E_i-E_j$ with E_i denoting the ith eigenenergy of the unperturbed Hamiltonian, and $\boldsymbol{r}$ and $\boldsymbol{\pi}=-i\partial/\partial\boldsymbol{r}$ the position and momentum, respectively, of the electron (bare mass m_0 and charge $-e$). Furthermore, the matrix element of an operator O between the unperturbed eigenstates $|i\rangle$ and $|j\rangle$ is denoted as $O_{ij}=\langle i|O|j\rangle$. The second equality of Eq. (2) holds for interband polarization.

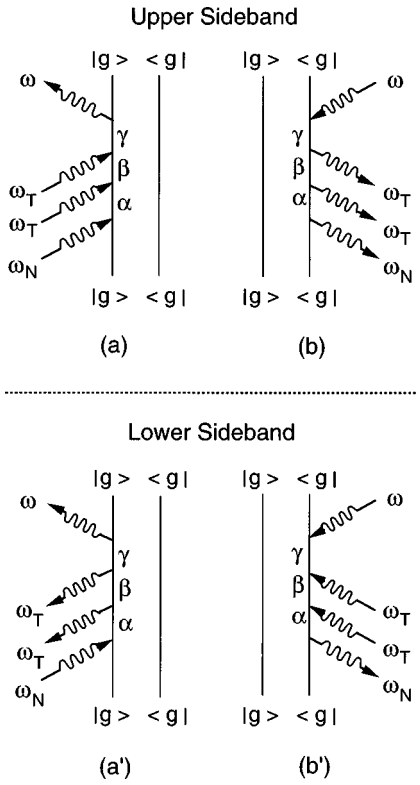

FIG. 1. Feynman diagrams for the density matrix describing the generation of the upper $(\omega_N+2\omega_T)$ sideband [(a) and (b)] and the lower $(\omega_N-2\omega_T)$ sideband [(a′) and (b′)]. While the diagrams (a) and (a′) have resonances, (b) and (b′) are nonresonant and are neglected in our calculations.

Let $H_N\propto E(\omega_N)$ and $H_T\propto E(\omega_T)$ be the interaction Hamiltonians describing the interaction of the electron system with the NIR and THz fields, respectively, and separate $H_{N,T}$ into positive and negative frequency parts as $H_{N,T}(t)=H_{N,T}^{(+)}\exp(-i\omega_{N,T}t)+H_{N,T}^{(-)}\exp(i\omega_{N,T}t)$. Applying the Feynman rule[16] to Fig. 1(a), and inserting the resulting expression of ρ_{ab} into Eq. (2), we obtain

$$\boldsymbol{P}^{(+)}(\omega_N\pm2\omega_T)=-\frac{ie}{m_0}\sum_{\alpha,\beta,\gamma}\frac{\boldsymbol{\pi}_{g\gamma}[H_T^{(\pm)}]_{\gamma\beta}[H_T^{(\pm)}]_{\beta\alpha}[H_N^{(+)}]_{\alpha g}}{\omega_{\gamma g}(\omega_N\pm2\omega_T-\omega_{\gamma g}+i\Gamma)(\omega_N\pm\omega_T-\omega_{\beta g}+i\Gamma)(\omega_N-\omega_{\alpha g}+i\Gamma)}, \tag{3}$$

where $\Gamma>0$ is a phenomenological damping factor. In deriving Eq. (3), the contribution of Fig. 1(b), which has no resonance, is neglected.

B. Magnetoexciton states

To obtain χ from Eq. (3), we first introduce a model for the unperturbed exciton and determine its eigenstates. The system we study is a MQW with GaAs wells (width L) separated by infinitely high potential barriers. Since the orbital degeneracy of the valence band (VB) at the Γ point is lifted by the confinement potential, both the conduction band (CB) and the valence band are assumed to be nondegenerate (aside from spin degeneracy) and parabolic with mass m_c and m_h, respectively $(m_c,m_h>0)$.[17] Thus, in considering the elec-

tronic structure of the system in the effective-mass approximation, we need the following band-edge (Γ point) Bloch functions: $|S\rangle|\uparrow\rangle$ and $|S\rangle|\downarrow\rangle$ for the CB and $-(|X\rangle+i|Y\rangle)|\uparrow\rangle/\sqrt{2}$ and $(|X\rangle-i|Y\rangle)|\downarrow\rangle/\sqrt{2}$ for the VB.[18] Here $|S\rangle$ and $\{|X\rangle,|Y\rangle,|Z\rangle\}$ are cell-periodic functions transforming like atomic s and p functions under the tetrahedral group at the Γ point, and $|\uparrow\rangle$ and $|\downarrow\rangle$ denote spin-up and -down functions of spin 1/2. We represent these Bloch functions as $\Phi_{\mathrm{CB},\sigma}(\boldsymbol{r})$ and $\Phi_{\mathrm{VB},\sigma}(\boldsymbol{r})$ with $\sigma=1$ (-1) for spin up (down).

In a quantum well, confinement quantizes electronic motion $\|z$ into subbands, and a magnetic field quantizes these subbands into discrete LL's. We neglect the spin Zeeman effect for simplicity: therefore, the LL's are spin degenerate. In the effective-mass approximation, we can take account of the confinement, and the magnetic field, and also of the e-h Coulomb attraction in terms of envelope functions that multiply the Bloch functions. Below, we outline the procedures followed to obtain these envelope functions, leaving the details to Appendix A.

The ground state $|g\rangle$ is simply the e-h vacuum with all VB (CB) LL's occupied (empty). As for the excited states, we only need to consider states with a single e-h pair with zero center-of-mass momentum and relative angular momentum $\ell_z=0,1,-1$. If we neglect the e-h Coulomb interaction H_c for the moment, the wave functions of these states can be written as

$$\frac{1}{\sqrt{S}}\langle\overline{\boldsymbol{r}}|N-1,N-1\rangle\zeta(z_e)\zeta(z_h)\Phi_{\mathrm{CB},\sigma}(\boldsymbol{r}_e)[K\Phi_{\mathrm{VB},\sigma}(\boldsymbol{r}_h)]$$

$$(\ell_z=0), \tag{4a}$$

$$\frac{1}{\sqrt{S}}\langle\overline{\boldsymbol{r}}|N-1,N\rangle\zeta(z_e)\zeta(z_h)\Phi_{\mathrm{CB},\sigma}(\boldsymbol{r}_e)[K\Phi_{\mathrm{VB},\sigma}(\boldsymbol{r}_h)]$$

$$(\ell_z=1), \tag{4b}$$

$$\frac{1}{\sqrt{S}}\langle\overline{\boldsymbol{r}}|N,N-1\rangle\zeta(z_e)\zeta(z_h)\Phi_{\mathrm{CB},\sigma}(\boldsymbol{r}_e)[K\Phi_{\mathrm{VB},\sigma}(\boldsymbol{r}_h)]$$

$$(\ell_z=-1), \tag{4c}$$

where K is the time-reversal operator, $\boldsymbol{r}_e=(x_e,y_e,z_e)$ and $\boldsymbol{r}_h=(x_h,y_h,z_h)$ are the coordinates of the electron and hole, respectively, and S is the area of the well. Furthermore, $\boldsymbol{r}=\boldsymbol{r}_e-\boldsymbol{r}_h$ is the e-h relative coordinate, and a bar over a vector signifies its projection onto the x-y (well) plane, i.e., $\overline{\boldsymbol{r}}=(x,y,0)$. The $\langle\overline{\boldsymbol{r}}|NN'\rangle$ is the envelope function describing the relative motion of the uncorrelated e-h pair with the electron (hole) occupying Landau level N (N'). Equations (4) are based on the assumption that $L\lesssim\epsilon/\mu e^2$ [= exciton Bohr radius $\sim$100 Å in GaAs; $\mu=(1/m_e+1/m_h)^{-1}$ is the reduced mass], so that the envelope functions are separable into z-dependent parts and in-layer parts (depending on x,y only) and further that only the ground subband [wave function $\zeta(z)$] needs to be considered.

The inclusion of the e-h Coulomb attraction (exciton effect) leads to the mixing of the functions of Eqs. (4) with different N but the same ℓ_z. Equations (4) are now replaced by

$$|\alpha\sigma\rangle=\frac{1}{\sqrt{S}}G_\alpha(\overline{\boldsymbol{r}})\zeta(z_e)\zeta(z_h)\Phi_{\mathrm{CB},\sigma}(\boldsymbol{r}_e)[K\Phi_{\mathrm{VB},\sigma}(\boldsymbol{r}_h)], \tag{5}$$

with

$$G_{s,i}(\overline{\boldsymbol{r}})=\sum_{n=1}^{\infty}c_n^{s,i}\langle\overline{\boldsymbol{r}}|n-1,n-1\rangle, \tag{6a}$$

$$G_{p(-),i}(\overline{\boldsymbol{r}})=\sum_{n=1}^{\infty}c_n^{p(-),i}\langle\overline{\boldsymbol{r}}|n-1,n\rangle, \tag{6b}$$

$$G_{p(+),i}(\overline{\boldsymbol{r}})=\sum_{n=1}^{\infty}c_n^{p(+),i}\langle\overline{\boldsymbol{r}}|n,n-1\rangle. \tag{6c}$$

Here, $(c_1^{\cdots,i},c_2^{\cdots,i},\ldots)$ is the ith eigenvector of the matrix of the unperturbed exciton Hamiltonian H_0 [Eq. (A10)] in the basis of Eqs. (4a), (4b), or (4c), and the low-field hydrogenic notation [$1s$,$2s$,$3s$, ..., $2p(\pm)$,$3p(\pm)$,$4p(\pm)$, ..., etc.] is used to label magnetoexciton states.

Having specified the unperturbed eigenstates, we can evaluate the transition matrix elements that appear in the numerator of Eq. (3). In the effective-mass approximation, H_N and H_T operate, respectively, on the Bloch part and the envelope function part of the electron wave function and, therefore, need separate treatments. Using the vector potential $\boldsymbol{A}_N=-c\int\boldsymbol{E}_N dt$ in $H_N=(e/cm_0)\boldsymbol{A}_N\cdot\boldsymbol{\pi}$, one obtains

$$H_N=-(ie/m_0\omega_N)(\boldsymbol{E}_N^{(+)}e^{-i\omega_N t}-\boldsymbol{E}_N^{(-)}e^{i\omega_N t})\cdot\boldsymbol{\pi}. \tag{7}$$

The matrix element of $\boldsymbol{\pi}$ between $|\alpha\sigma\rangle$ as given by Eq. (5) and the vacuum $|g\rangle$ can be obtained by a standard procedure.[19] The result reads

$$\boldsymbol{\pi}_{g,\alpha\sigma}=\frac{1}{\sqrt{2}}G_\alpha(0)R\,\boldsymbol{\eta}_\sigma, \tag{8}$$

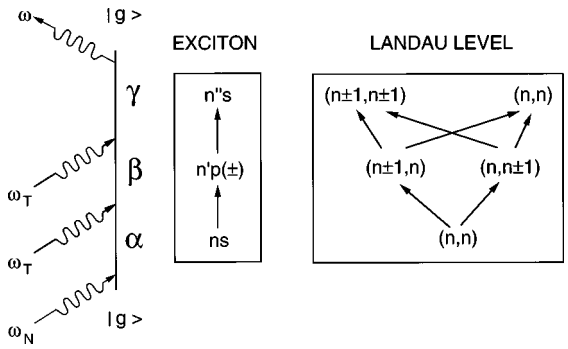

FIG. 2. Possible intermediate states α, β, and γ when the e-h Coulomb interaction is included (''exciton'' picture) and neglected (''Landau level'' picture).

where $R=-i\langle X|\pi_x|S\rangle=-i\langle Y|\pi_y|S\rangle$ is the interband matrix element, and $\boldsymbol{\eta}_\sigma=(\eta_{x\sigma},\eta_{y\sigma})$ is a spin-dependent factor defined by $\eta_{x\sigma}=-i\sigma$ and $\eta_{y\sigma}=-1$. Inserting this into Eq. (7), we get

$$[H_N^{(\pm)}]_{\alpha\sigma,g}=\frac{\mp ieR}{\sqrt{2}m_0\omega_N}G_\alpha(0)^*\boldsymbol{E}_N^{(\pm)}\cdot\boldsymbol{\eta}_\sigma^*. \tag{9}$$

The derivation of the matrix elements of H_T needs a more elaborate treatment and is discussed in Appendix A. The final result is

$$[H_T^{(\pm)}]_{\gamma\sigma,\beta\sigma'}=\pm\frac{ie}{\mu\omega_T}(E_x^{(\pm)}A_{\gamma\beta}^x+E_y^{(\pm)}A_{\gamma\beta}^y)\delta_{\sigma\sigma'}, \tag{10}$$

with

$$A_{\gamma\beta}^x=i\int d^2\overline{r}\,\overline{G}_\gamma(\overline{\boldsymbol{r}})^*\left(\partial/\partial x-\frac{i\mu}{2\xi\ell^2}y\right)G_\beta(\overline{\boldsymbol{r}}), \tag{11a}$$

$$A_{\gamma\beta}^y=i\int d^2\overline{r}\,\overline{G}_\gamma(\overline{\boldsymbol{r}})^*\left(\partial/\partial y+\frac{i\mu}{2\xi\ell^2}x\right)G_\beta(\overline{\boldsymbol{r}}), \tag{11b}$$

where $\ell=\sqrt{c/Be}$ and $\xi=(1/m_e-1/m_h)^{-1}$.

C. Expression for susceptibility χ_{ijkl}

Inserting Eqs. (7)–(10) into Eq. (3) and using the definition of χ [Eq. (1)], we get

$$\chi_{ijkl}=\frac{Ne^4R^2\Xi_{il}}{2m_0^2\mu^2\omega_T^2\omega_N}\sum_{\alpha\beta\gamma}\frac{A_{\gamma\beta}^jA_{\beta\alpha}^k[G_\alpha(0)]^*G_\gamma(0)}{\omega_{\gamma g}(\omega_N\pm2\omega_T-\omega_{\gamma g}+i\Gamma)(\omega_N\pm\omega_T-\omega_{\beta g}+i\Gamma)(\omega_N-\omega_{\alpha g}+i\Gamma)}, \tag{12}$$

where the upper (lower) sign corresponds to the upper (lower) sideband, and $\Xi_{il}=\Sigma_{\sigma=\pm1}\eta_{i\sigma}(\eta_{l\sigma})^*$. In Eq. (12), the number of well layers per unit thickness N is included. Throughout this paper, we set N^{-1} (MQW period) to be 250 Å.[11–15]

In the $B\to\infty$ limit, the Coulomb interaction becomes negligible and $c_n^{\ldots,i}=\delta_{ni}$. Thus the e-h pair state α, β, or γ in Eq. (12) becomes a product of electron and hole Landau wave functions. The possible perturbation processes in this LL picture is depicted also in Fig. 2. After some algebra (Appendix B), Eq. (12) reduces to

$$\begin{aligned}\chi_{ijkl}=\frac{NB^2e^6R^2\Xi_{il}}{8\pi c^2m_0^2\omega_T^2\omega_N}\sum_{n=0}^{\infty}{\sum_{n'=n\pm1}}'\Bigg[&\frac{\max(n,n')\beta_{nn'}^j\beta_{n'n}^k}{m_e^2\omega_{nn}(\omega_N\pm2\omega_T-\omega_{nn}+i\Gamma)(\omega_N\pm\omega_T-\omega_{n'n}+i\Gamma)(\omega_N-\omega_{nn}+i\Gamma)}\\&+\frac{\max(n,n')\beta_{n'n}^j\beta_{nn'}^k}{m_h^2\omega_{nn}(\omega_N\pm2\omega_T-\omega_{nn}+i\Gamma)(\omega_N\pm\omega_T-\omega_{nn'}+i\Gamma)(\omega_N-\omega_{nn}+i\Gamma)}\\&-\frac{\max(n,n')\beta_{nn'}^j\beta_{n'n}^k}{m_em_h\omega_{n'n'}(\omega_N\pm2\omega_T-\omega_{n'n'}+i\Gamma)(\omega_N\pm\omega_T-\omega_{n'n}+i\Gamma)(\omega_N-\omega_{nn}+i\Gamma)}\\&-\frac{\max(n,n')\beta_{n'n}^j\beta_{nn'}^k}{m_em_h\omega_{n'n'}(\omega_N\pm2\omega_T-\omega_{n'n'}+i\Gamma)(\omega_N\pm\omega_T-\omega_{nn'}+i\Gamma)(\omega_N-\omega_{nn}+i\Gamma)}\Bigg],\end{aligned} \tag{13}$$

where $\beta_{n,n\pm1}^x=\mp i$, $\beta_{n,n\pm1}^y=1$ and $\omega_{nn'}=E_g+\omega_{ce}(n+1/2)+\omega_{ch}(n'+1/2)$ with $n,n'=0,1,2,\ldots$. (The prime over the n' summation indicates $n'\geqslant0$.)

It can be shown that χ_{ijkl} as given by Eq. (12) or (13) vanishes if $i\neq l$ and the nonvanishing elements obey the symmetry relations: $\chi_{xxxx}=\chi_{xyyx}=\chi_{yxxy}=\chi_{yyyy}$, $\chi_{xxyx}=-\chi_{xyxx}=\chi_{yxyy}=-\chi_{yyxy}$.

D. Resonance structure of χ_{ijkl}

The zeroes of the denominator of Eq. (12) determine resonances. For the upper sideband, these resonances are

$$\omega_N=\omega_{1s},\omega_{2s},\ldots, \tag{14a}$$

$$\omega_N+\omega_T=\omega_{2p(\pm)},\omega_{3p(\pm)},\ldots, \tag{14b}$$

$$\omega_N+2\omega_T=\omega_{1s},\omega_{2s},\ldots. \tag{14c}$$

Note that the left-hand side of Eq. (14c) is equal to the sideband frequency. If two of the above conditions are simultaneously satisfied, we have a double resonance. Limiting ourselves to the case that the first condition [Eq. (14a)] is satisfied, a double resonance occurs when

$$\omega_N=\omega_{ns}, \tag{15a}$$

$$\omega_T=\omega_{n'p(\pm)}-\omega_{ns}, \tag{15b}$$

or

$$\omega_N=\omega_{ns}, \tag{16a}$$

$$\omega_T=(\omega_{n''p(\pm)}-\omega_{ns})/2 \tag{16b}$$

with $n\geqslant1$ and $n',n''\geqslant2$.

The resonance conditions for the lower sideband are obtained by simply replacing ω_T by $-\omega_T$ in Eqs. (14)–(16).

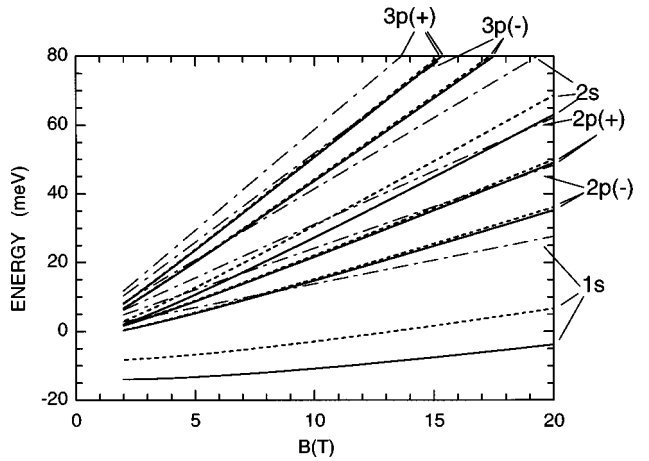

FIG. 3. Calculated magnetoexciton energies for $L=100$ Å (dashed curves) and $L=0$ (solid curves). For comparison, the energies calculated without the Coulomb interaction are plotted by dash-dotted curves.

E. THz polarization dependence of sideband intensity

Suppose the THz radiation is circularly polarized ($E_y=\pm iE_x$). Then the sideband intensity vanishes because $\Sigma_{jk}\chi_{ijkl}E_jE_k=0$ due to the symmetries $\chi_{ixxl}=\chi_{iyyl}$ and $\chi_{ixyl}=-\chi_{iyxl}$ mentioned in Sec. II C.

This is more readily understood from Fig. 2. The generation of the upper sideband, for example, involves the absorption of two THz photons. Assuming that these photons are right circularly polarized, their absorption can only *increase* the exciton angular momentum, i.e., $s\rightarrow p(+)$ and $p(-)\rightarrow s$ transitions are allowed but $s\rightarrow p(-)$ and $p(+)\rightarrow s$ are forbidden. As a result, one of the two THz transitions is forbidden, leading to vanishing sideband intensity. The same conclusion holds also for left circular polarization. If, however, the THz photons are linearly polarized (50%–50% mixture of right and left curcular polarizations), both of the two THz transitions are allowed. Obviously, the sideband intensity is maximum for linear polarization. This result is fully supported by experiment.[15]

III. NUMERICAL RESULTS

A. Magnetoexciton spectrum

We diagonalize numerically the unperturbed exciton Hamiltonian [Eq. (A10)]. The material parameters used are $m_e=0.067$, $m_h=1/(\gamma_1+\gamma_2)$ with $\gamma_1=6.85$ and $\gamma_2=2.1$, $\epsilon=12.5$, and $R=1.294\times10^{-19}$ g cm/s. Figure 3 presents the calculated exciton eigenenergies for $L=100$ Å (dashed curves) and $L=0$ (solid curves). For $L=100$ Å, 40 basis functions were found to be sufficient for $B>2$ T. The two-dimensional limit ($L=0$), which requires a much larger basis set,[20] was calculated using up to 300 basis functions. For comparison, the energies obtained without *e-h* Coulomb attraction (Landau levels) are plotted by dash-dotted curves.

The energies and wave functions thus obtained are used in Eqs. (12) or (13) to get χ_{ijkl}. Hereafter, we limit our discussion to its diagonal element $\chi\equiv\chi_{xxxx}$.

B. Magnetic-field dependence of χ

The upper panel of Fig. 4 presents the modulus of χ for the upper sideband calculated as a function of B with ω_N set equal to ω_{1s} *at each value of* B. Here ω_T is fixed at 115 cm^{-1} and $L=100$ Å. The solid and dashed lines are plots with and without the *e-h* attraction, respectively. Both curves exhibit three main peaks, in qualitative agreement with experiment (lower panel of Fig. 4), but the curve with *e-h* attraction gives much better overall agreement. It, however, fails to reproduce the precise resonance positions B_{res}. This discrepancy, we believe, is mainly due to our neglect of the valence-band complexity. The resonant magnetic fields B_{res} deduced by using in Eq. (12) the exciton energies calculated by Bauer and Ando,[21] who took into account the valence-band nonparabolicity, are indicated in Fig. 4 by arrows at the top. Agreement with experiment is indeed better compared to our parabolic approximation.

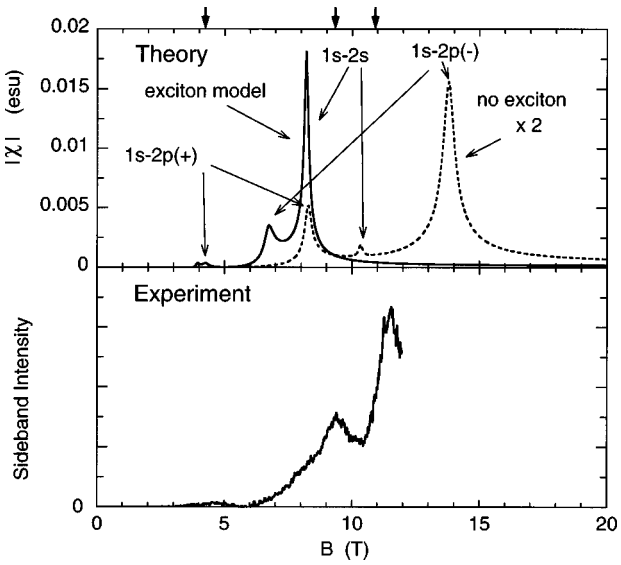

FIG. 4. The upper panel presents $|\chi|=|\chi_{xxxx}|$ for the upper sideband calculated as a function of B with ω_N tuned to ω_{1s} at each value of B. The parameters used are $\omega_T=115$ cm^{-1}, $L=100$ Å, and $\Gamma=0.2$ meV. The solid line denotes the result which takes into account the *e-h* Coulomb attraction (exciton model), while the dashed line neglects it. Experimental sideband intensity is presented in the lower panel.

Since the first resonance condition Eq. (14a) is satisfied ($\omega_N=\omega_{1s}$) at each magnetic field, the peaks in Fig. 4 represent double resonances as given by Eqs. (15b) and (16b), and are attributed to intraexciton transitions $1s$-$2p(\pm)$ and $1s$-$2s$.

In Fig. 4, the peak heights increase with B. This reflects the B dependence of the numerator of Eq. (12), which is governed by the factors $A_{\alpha\alpha'}$ and $G_\alpha(0)$. In the limit of vanishing Coulomb interaction (or $B\rightarrow\infty$), $A_{\alpha\alpha'}\sim\sqrt{B}$ and $G_\alpha(0)\sim\sqrt{B}$ [Eqs. (B1) and (B2)]. Therefore, $A_{\gamma\beta}A_{\beta\alpha}[G_\alpha(0)]^*G_\gamma(0)\sim B^2$, which accounts for the prefactor B^2 in Eq. (13). Even in the presence of the Coulomb interaction, $A_{\gamma\beta}A_{\beta\alpha}[G_\alpha(0)]^*G_\gamma(0)$ is roughly proportional to B^2 for $B>2$ T. This $\sim B^2$ variation of the numerator of Eq. (12) explains the increasing peak height as B increases. However, χ at double resonance is also affected by the denominator, i.e., how far away the third resonance is. This can cause significant deviation from the simple $\sim B^2$ dependence.

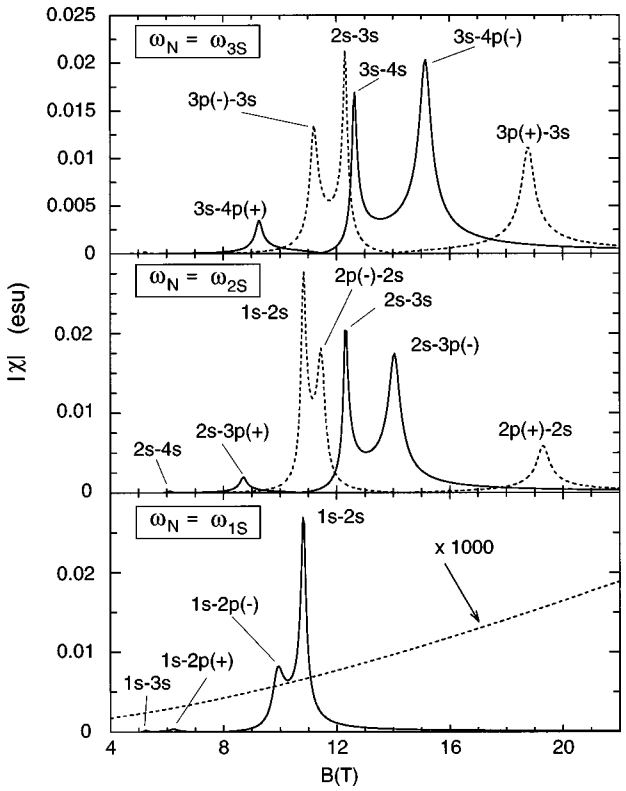

FIG. 5. Calculated $|\chi|$ for the upper (solid line) and the lower (dashed line) sideband for ω_N tuned to $1s$, $2s$, and $3s$ exciton absorption energies. The parameters used are $\omega_T = 144\ \mathrm{cm}^{-1}$, $L = 100$ Å, and $\Gamma = 0.2$ meV.

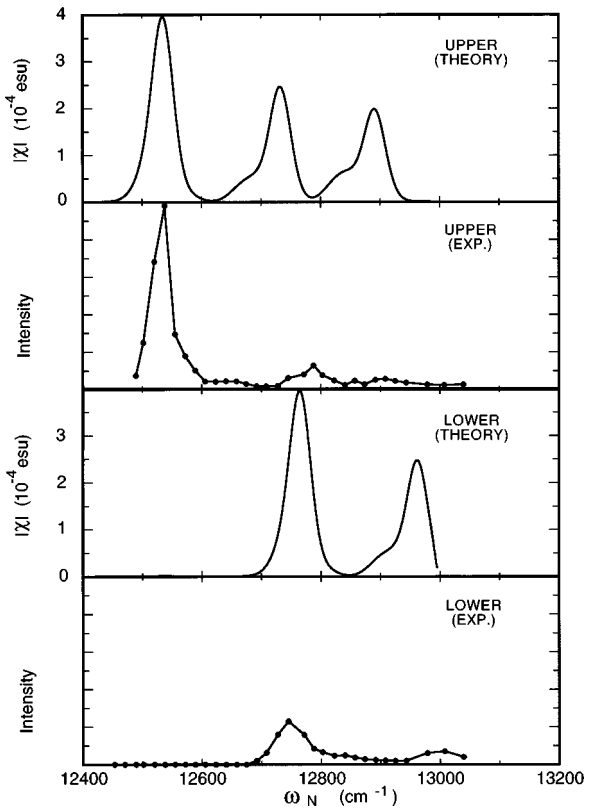

FIG. 6. Calculated $|\chi|$ vs ω_N for both the upper sideband (top panel) and the lower sideband (second panel from the bottom). The parameters used are $\omega_T = 115\ \mathrm{cm}^{-1}$, $L = 100$ Å, $\Gamma = 0.2$ meV, and B is chosen to be 6.705 T, which corresponds to the middle peak in the upper panel of Fig. 4. Presented immediately below the theoretical results are the corresponding experiments.

The bottom panel of Fig. 5 plots the intensities of both the upper and lower sidebands (solid and dashed curves, respectively) with ω_N tuned, as before, to ω_{1s}. (The other parameters are $\omega_T = 144\ \mathrm{cm}^{-1}$ and $L = 100$ Å. Here and afterwards, all the numerical results include the e-h attraction.) Unlike the upper sideband, the lower sideband has no resonance and is smaller by three orders of magnitude than the upper. This is readily explained by Eqs. (15) and (16), with the sign of ω_T reversed. Since $\omega_{ns} = \omega_{1s}$, the right-hand sides of Eqs. (15b) and (16b) are positive, while the left-hand sides are negative, leaving no chance for equalities to hold.

This is no longer the case if ω_N is tuned to a higher exciton absorption peak. This is exemplified in the middle and upper panels of Fig. 5, illustrating the cases $\omega_N = \omega_{2s}$ and ω_{3s}, respectively. The many peaks originate from various s-p and s-s intraexciton transitions, demonstrating the usefulness of the sideband generation as a new magnetoexciton spectroscopy.

C. Radiation frequency dependence of χ

χ also exhibits resonances as a function of ω_N. The results of the calculation for $\omega_T = 115\ \mathrm{cm}^{-1}$ and $L = 100$ Å are presented in Fig. 6 for both the upper and lower sidebands, together with corresponding experiments. To improve agreement with experiment, we have broadened the $\chi(\omega_N)$ obtained from Eq. (12) by convoluting it with a Gaussian of half-width 3 meV. The overall agreement with experiment is satisfactory.

In Fig. 6, the peaks for the upper sideband can be roughly ascribed, from left to right, to $1s$, $2s$, and $3s$ exciton resonances. As for the lower sideband, the lowest peak is the $2s$ resonance, because there is no $1s$ resonance for the reason stated previously. (This is a rough interpretation, because each of the broadened peaks actually consists of many resonant peaks.)

Figure 7 plots the resonant magnetic fields versus ω_T with ω_N tuned to ω_{1s}. As ω_T changes, the $1s$-$2p(-)$ and $1s$-$2s$ peaks are seen to switch. This indicates that the order of the peaks is a subtle issue and may only be determined from a sophisticated magnetoexciton theory taking fully into account the valence-band nonparabolicity.

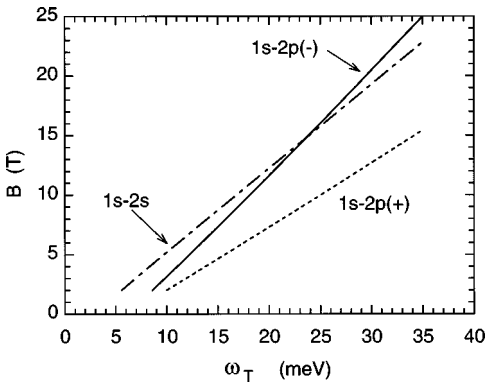

FIG. 7. Resonant magnetic fields for the upper sideband, calculated for various ω_T, are plotted vs ω_T. Here $\omega_N = \omega_{1s}$, $L = 100$ Å, and $\Gamma = 0.2$ meV.

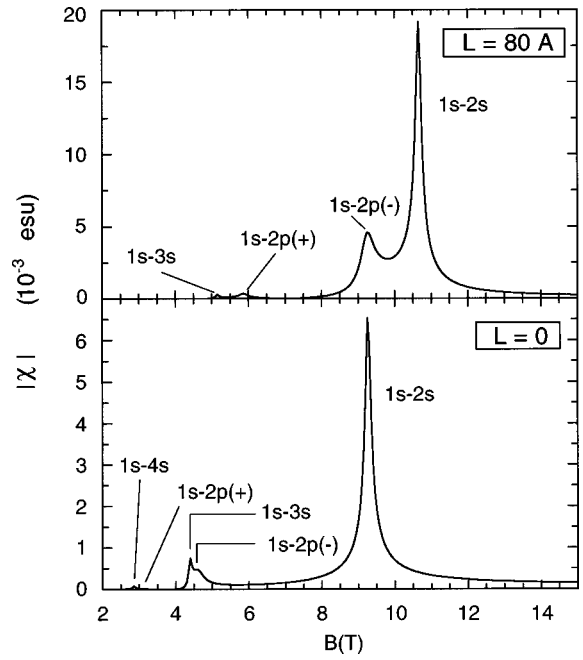

FIG. 8. $|\chi|$ for the upper sideband calculated as a function of B. The results for $L=80$ Å and 0 (2D limit) are compared.

D. Well width dependence of χ

Figure 8 compares $|\chi|$ versus B for $L=80$ Å and 0 (two-dimensional limit) for $\omega_N=\omega_{1s}$ and $\omega_T=144$ cm^{-1}. Although all the peaks move towards larger B as L increases, the s-p peaks move faster than the s-s peaks. For $L=80$ Å, the dominant resonances result from transitions between adjacent symmetry-allowed states [$1s$-$2p(\pm)$ and $1s$-$2s$]. As L decreases, transitions to more distant levels (e.g., $1s$-$3s$) become stronger as seen in the larger $1s$-$3s$ and $1s$-$4s$ peaks for $L=0$. This is understood from the fact that the Coulomb interaction becomes more important as $L\rightarrow 0$. If the Coulomb interaction is negligible, transitions take place only between adjacent exciton levels (i.e., starting from $1s$, only transitions to $2p(\pm)$ and $2s$ are allowed). This is a consequence of the well-known selection rule between Landau levels $\Delta n=\pm 1$. Thus transitions to more distant states such as $1s$-$3s$ contribute only when the Coulomb interaction is sufficiently strong, i.e., if L or B is small.

IV. CONCLUDING REMARKS

Our simple perturbation theory based on a magnetoexciton model provides semiquantitative explanations to all the main characteristics of the sidebands observed experimentally. Although some qualitative features of the experiment may be explained without considering the e-h Coulomb attraction, we found it essential to include the exciton effect.

Our magnetoexciton calculation was based on a simple parabolic approximation. One can improve the results by using in Eq. (12) the wave functions and energies obtained from a more sophisticated exciton theory. Thus Eq. (12) will serve as a useful test of magnetoexciton theories.

We have shown how the resonance structure of the sidebands can be related, with the aid of our theory, to exciton internal transitions. This demonstrates the usefulness of the sideband generation phenomenon as a new magnetoexciton spectroscopy. Obviously this sideband spectroscopy should have a wide range of applications. Especially interesting target systems are semiconductor nanostructures such as quantum dots.

In this paper, we have focused our discussion on the $\omega_N\pm 2\omega_T$ sidebands for which experiment has already generated much knowledge. As for the weaker $\omega_N\pm 4\omega_T$ sidebands,[14] we believe that they can also be described by a straightforward generalization of our theory.

ACKNOWLEDGMENTS

The authors are indebted to T. Ando, J. Černe, M. Y. Su, M. S. Sherwin, and S. J. Allen, Jr., for valuable discussions.

APPENDIX A: DETAILS OF THE MAGNETOEXCITON CALCULATION

Taking the symmetric gauge for the magnetic field $\boldsymbol{B}\|z$, the effective-mass Hamiltonian of a magnetoexciton interacting with THz radiation (vector potential $\boldsymbol{A}_T\perp z$) reads

$$H'=\sum_{i=e,h}\frac{1}{2m_i}\left(\overline{\boldsymbol{p}}_i-\frac{e_i}{2c}\boldsymbol{B}\times\overline{\boldsymbol{r}}_i-\frac{e_i}{c}\boldsymbol{A}_T\right)^2+\sum_{i=e,h}\left(\frac{p_{iz}^2}{2m_i}+V(z_i)\right)-\frac{e^2}{\epsilon r},\tag{A1}$$

where $\boldsymbol{r}_e=(x_e,y_e,z_e)$ and $\boldsymbol{r}_h=(x_h,y_h,z_h)$ denote the electron and hole coordinates, respectively, $\boldsymbol{p}_{e,h}=-i\partial/\partial\boldsymbol{r}_{e,h}$, $\boldsymbol{r}=\boldsymbol{r}_e-\boldsymbol{r}_h$, $e>0$ the elementary charge, and the projection of a vector onto the well plane is indicated by an overbar. Furthermore, ϵ is the static dielectric constant, m_i and e_i the effective mass and the charge, respectively, of the electron ($i=e$) and hole ($i=h$), and c the velocity of light in vacuum. In Eq. (A1), the spin Zeeman effect is neglected, and therefore spin indices are suppressed throughout this appendix.

Performing a unitary transformation

$$U=\exp[(-ie/2c)\boldsymbol{B}\cdot(\overline{\boldsymbol{r}}_e\times\overline{\boldsymbol{r}}_h)]$$

on H' and assuming the exciton center-of-mass momentum along the well to vanish, we obtain

$$H=UH'U^{\dagger}=H_0+H_T,\tag{A2a}$$

$$H_0=H_{2D}+H_{\perp}+H_c,\tag{A2b}$$

with

$$H_{2D}=\sum_{i=e,h}\frac{1}{2m_i}\left(\overline{\boldsymbol{p}}-\frac{e_i}{2c}\boldsymbol{B}\times\overline{\boldsymbol{r}}\right)^2,\tag{A3a}$$

$$H_{\perp}=\sum_{i=e,h}\left(\frac{p_{iz}^2}{2m_i}+V(z_i)\right),\tag{A3b}$$

$$H_c=-\frac{e^2}{\epsilon r},\tag{A3c}$$

$$H_T=\frac{e}{\mu c}\boldsymbol{A}_T\cdot\overline{\boldsymbol{p}}+\frac{e^2}{2\xi c^2}\boldsymbol{A}_T\cdot(\boldsymbol{B}\times\overline{\boldsymbol{r}}).\tag{A3d}$$

Here $\boldsymbol{p}=-i\partial/\partial\boldsymbol{r}$, $\mu^{-1}=m_e^{-1}+m_h^{-1}$, and $\xi^{-1}=m_e^{-1}-m_h^{-1}$. The term quadratic in A_T is irrelevant and therefore ignored. As for the confinement, we assume a simple hard-wall potential:

$$V(z)=\begin{cases}0, & -L/2<z<L/2\\ \infty, & \text{otherwise.}\end{cases} \tag{A4}$$

Now we introduce creation and annihilation operators to describe the dynamics in the x-y plane:[20,22]

$$x=\frac{\ell}{\sqrt{2}}(a+a^\dagger+b+b^\dagger), \tag{A5a}$$

$$y=\frac{i\ell}{\sqrt{2}}(a-a^\dagger-b+b^\dagger), \tag{A5b}$$

$$\partial/\partial x=\frac{1}{2\sqrt{2}\ell}(a-a^\dagger+b-b^\dagger), \tag{A5c}$$

$$\partial/\partial y=\frac{i}{2\sqrt{2}\ell}(a+a^\dagger-b-b^\dagger), \tag{A5d}$$

where $\ell=\sqrt{c/Be}$ is the magnetic length. The operators a and b satisfy Bose commutation relations, and a and $a^\dagger$ commute with b and $b^\dagger$. This transforms H_{2D} into

$$H_{2D}=\omega_{ce}(a^\dagger a+\tfrac{1}{2})+\omega_{ch}(b^\dagger b+\tfrac{1}{2}), \tag{A6}$$

where $\omega_{ce}=eB/m_ec$ and $\omega_{ch}=eB/m_hc$ are the electron and hole cyclotron frequencies, respectively. Equation (A6) shows that $a^\dagger a$ and $b^\dagger b$ are the Landau indices for the electron and hole, respectively. Denoting the eigenfunctions of H_{2D} as $|n(=a^\dagger a),m(=b^\dagger b)\rangle$ $(n,m=0,1,2,\ldots)$ and assuming that the barrier confinement is comparable or stronger than the e-h Coulomb confinement, i.e., $L\lesssim\epsilon/\mu e^2$ (exciton Bohr radius), we construct the following approximate basis functions:

$$|n,m\rangle\rangle=|n,m\rangle\zeta(z_e)\zeta(z_h), \tag{A7}$$

where $\zeta(z)$ is the lowest eigenfunction of $H_\perp$ $(|z|<L/2)$,

$$\zeta(z)=\sqrt{\frac{2}{L}}\cos\frac{\pi z}{L}. \tag{A8}$$

Now we diagonalize the quasi-2D exciton Hamiltonian $H_0=H_{2D}+H_\perp+H_c$ using $\{|n,m\rangle\rangle\}$ as the basis. Since H_0 conserves the z component of the exciton angular momentum $\ell_z=a^\dagger a-b^\dagger b$,[22] diagonalization can be carried out separately in the $\ell_z=0,-1,1$ subspaces [or s, $p(-)$ and $p(+)$ subspaces in the low-B hydrogenic notation]. These subspaces are spanned by the following functions $(n=1,2,3,\ldots)$:

$$\psi_n^s=|n-1,n-1\rangle\rangle, \tag{A9a}$$

$$\psi_n^{p(-)}=|n-1,n\rangle\rangle, \tag{A9b}$$

$$\psi_n^{p(+)}=|n,n-1\rangle\rangle. \tag{A9c}$$

The matrix elements of H_0 are

$$\begin{aligned}\langle\langle n',n'+s|H_0|n,n+s\rangle\rangle&=\delta_{nn'}[E_{0z}+\omega_{ce}(n+1/2)+\omega_{ch}(n+s+1/2)]\\&-\frac{e^2}{\epsilon}\left\langle\left\langle n',n'+s\left|\frac{1}{\sqrt{r^2+z^2}}\right|n,n+s\right\rangle\right\rangle,\end{aligned} \tag{A10}$$

with z-quantization energy:

$$E_{0z}=\frac{\pi^2}{2\mu L^2}. \tag{A11}$$

Using

$$\frac{1}{\sqrt{r^2+z^2}}=\frac{1}{\ell}\int\frac{d^2q}{2\pi q}e^{-q|z|/\ell}e^{i\boldsymbol{q}\cdot\bar{\boldsymbol{r}}/\ell}, \tag{A12}$$

the Coulomb matrix elements in Eq. (A10) can be transformed into

$$\begin{aligned}\left\langle\left\langle n',n'+s\left|\frac{1}{\sqrt{r^2+z^2}}\right|n,n+s\right\rangle\right\rangle&\\=\frac{1}{\ell}\int\frac{d^2q}{2\pi q}\langle n',n'+s|e^{i\boldsymbol{q}\cdot\bar{\boldsymbol{r}}/\ell}|n,n+s\rangle I(q/\ell),&\end{aligned} \tag{A13}$$

with

$$I(q)=\int_{-L/2}^{L/2}dz_e\int_{-L/2}^{L/2}dz_h\zeta(z_e)^2\zeta(z_h)^2e^{-q|z_e-z_h|}. \tag{A14}$$

Integration of Eq. (A14) with Eq. (A8) is straightforward. The resulting formula, which is quite lengthy, is found to be well approximated by

$$I(q)=\frac{3}{qL}-\frac{9}{2q^2L^2}+\frac{9}{2q^2L^2}e^{-2qL/3}. \tag{A15}$$

On the other hand, by transforming the first factor in the integrand of Eq. (A13) using Eqs. (A5), Eq. (A13) can be reduced to[20,22]

$$\begin{aligned}\left\langle\left\langle n',n'+s\left|\frac{1}{\sqrt{r^2+z^2}}\right|n,n+s\right\rangle\right\rangle&\\=\frac{1}{\sqrt{2}\ell}\sqrt{\frac{N!(N+s)!}{N'!(N'+s)!}}\int_0^\infty dxe^{-x}x^{N'-N-1/2}&\\\times L_N^{N'-N}(x)L_{N+s}^{N'-N}(x)I(\sqrt{2x}/\ell),&\end{aligned} \tag{A16}$$

where $N=\min(n,n')$, $N'=\max(n,n')$, and $L_m^{m'}(x)$ is a generalized Laguerre polynomial. In the 2D limit $(L\to0)$, $I(q)=1$ and Eq. (A16) can be further simplified by the Gauss formula.[23]

Diagonalization of the matrix of Eq. (A10) gives the eigenfunctions of H_0 in the form of the following linear combination:

$$\sum_n c_n^{\cdots,i}\psi_n^{\cdots}(\overline{\boldsymbol{r}}) = G_{\ldots,i}(\overline{\boldsymbol{r}})\zeta(z_e)\zeta(z_h), \quad \text{(A17)}$$

with

$$G_{s,i}(\overline{\boldsymbol{r}}) = \sum_n c_n^{s,i}\langle\overline{\boldsymbol{r}}|n-1,n-1\rangle, \quad \text{(A18a)}$$

$$G_{p(-),i}(\overline{\boldsymbol{r}}) = \sum_n c_n^{p(-),i}\langle\overline{\boldsymbol{r}}|n-1,n\rangle, \quad \text{(A18b)}$$

$$G_{p(+),i}(\overline{\boldsymbol{r}}) = \sum_n c_n^{p(+),i}\langle\overline{\boldsymbol{r}}|n,n-1\rangle. \quad \text{(A18c)}$$

Here $(c_1^{\cdots,i}, c_2^{\cdots,i}, \ldots)$ denotes the ith eigenvector of Eq. (A10), which we normalize to 1, i.e., $\Sigma_n|c_n^{\cdots,i}|^2=1$. This ensures that, if $\psi_n^{\cdots}(\overline{\boldsymbol{r}})$'s are normalized to 1 in the whole (2D) space, so do the exciton envelope functions $G_{\ldots,n}(\overline{\boldsymbol{r}})$.

To obtain $G_{s,i}(\overline{\boldsymbol{r}}=0)$, which we need to calculate the matrix elements of H_N [Eq. (9)], we note that $\langle\overline{\boldsymbol{r}}|n-1,n-1\rangle$ is an $\ell_z=0$ eigenfunction of H_{2D} [Eq. (A3a)].[22] Solving the corresponding Schrödinger equation in the coordinate representation, we get the normalized solutions:

$$\langle\overline{\boldsymbol{r}}|n-1,n-1\rangle = \frac{1}{\sqrt{2\pi}\ell}\exp\left(\frac{-\overline{r^2}}{4\ell^2}\right)L_{n-1}^{(0)}(\overline{r^2}/2\ell^2). \quad \text{(A19)}$$

Therefore

$$G_{s,i}(\overline{\boldsymbol{r}}=0) = \sum_n c_n^{s,i}\langle\overline{\boldsymbol{r}}=0|n-1,n-1\rangle = \frac{1}{\sqrt{2\pi}\ell}\sum_n c_n^{s,i}. \quad \text{(A20)}$$

Finally, the full envelope function, including the trivial center-of-mass part ($=1/\sqrt{S}$; S is the area of the well), reads

$$F_\alpha(\overline{\boldsymbol{r}}, \overline{\boldsymbol{R}}, z_e, z_h) = \frac{1}{\sqrt{S}}G_\alpha(\overline{\boldsymbol{r}})\zeta(z_e)\zeta(z_h), \quad \text{(A21)}$$

where α is shorthand for $\{s,i\}$, $\{p(-),i\}$, or $\{p(+),i\}$, and $\boldsymbol{R}$ is the center-of-mass coordinate. This function is normalized to unity according to $\int|F_\alpha|^2 d^2\overline{r}\,d^2\overline{R}\,dz_e dz_h=1$, where the $\overline{\boldsymbol{R}}$ integration cancels the S in the denominator.

Now we proceed to the calculation of the matrix elements of H_T. Inserting $\boldsymbol{A}_T=(-ic/\omega_T)(\boldsymbol{E}_T^{(+)}e^{-i\omega_T t}-\boldsymbol{E}_T^{(-)}e^{i\omega_T t})$ into H_T and taking its matrix element between F_γ and F_β, we get

$$[H_T^{(\pm)}]_{\gamma\beta} = \pm\frac{ie}{\mu\omega_T}(E_{Tx}^{(\pm)}A_{\gamma\beta}^x + E_{Ty}^{(\pm)}A_{\gamma\beta}^y), \quad \text{(A22)}$$

with

$$A_{\gamma\beta}^x = i\int d^2\overline{r}\,G_\gamma^*(\overline{\boldsymbol{r}})\left(\partial/\partial x - \frac{i\mu}{2\xi\ell^2}y\right)G_\beta(\overline{\boldsymbol{r}}), \quad \text{(A23a)}$$

$$A_{\gamma\beta}^y = i\int d^2\overline{r}\,G_\gamma^*(\overline{\boldsymbol{r}})\left(\partial/\partial y + \frac{i\mu}{2\xi\ell^2}x\right)G_\beta(\overline{\boldsymbol{r}}). \quad \text{(A23b)}$$

Using Eqs. (A18) and (A5), Eqs. (A23) can be reduced to

$$A_{\gamma\beta}^x = [A_{\beta\gamma}^x]^* = \frac{i}{2\sqrt{2}\ell}\sum_{n=1}^{\infty}\sqrt{n}[c_n^\gamma]^*(\lambda_e c_{n+1}^\beta - \lambda_h c_n^\beta), \quad \text{(A24a)}$$

$$A_{\gamma\beta}^y = [A_{\beta\gamma}^y]^* = -iA_{\gamma\beta}^x, \quad \text{(A24b)}$$

if γ is a $p(+)$ state and β is an s state, and

$$A_{\gamma\beta}^x = [A_{\beta\gamma}^x]^* = \frac{i}{2\sqrt{2}\ell}\sum_{n=1}^{\infty}\sqrt{n}[c_n^\gamma]^*(\lambda_h c_{n+1}^\beta - \lambda_e c_n^\beta), \quad \text{(A25a)}$$

$$A_{\gamma\beta}^y = [A_{\beta\gamma}^y]^* = iA_{\gamma\beta}^x, \quad \text{(A25b)}$$

if γ is a $p(-)$ state and β is an s state. Here $\lambda_e=2m_e/(m_h+m_c)$ and $\lambda_h=2m_h/(m_h+m_c)$.

APPENDIX B: $B\to\infty$ LIMIT

In this limit, $c_n^{\cdots,i}=\delta_{ni}$. Inserting this into Eq. (A20), we get

$$G_{s,i}(\overline{\boldsymbol{r}}=0) = \frac{1}{\sqrt{2\pi}\ell}. \quad \text{(B1)}$$

Transforming Eqs. (A24) and (A25) in the similar way, and using the LL representations for the states α, etc., as explained in the text, we get

$$A_{n'n,nn}^i = -\frac{\mu}{\sqrt{2}m_e\ell}\sqrt{\max(n,n')}\beta_{n'n}^i, \quad \text{(B2a)}$$

$$A_{nn',nn}^i = \frac{\mu}{\sqrt{2}m_h\ell}\sqrt{\max(n,n')}\beta_{n'n}^i, \quad \text{(B2b)}$$

$$A_{nn,n'n}^i = -\frac{\mu}{\sqrt{2}m_e\ell}\sqrt{\max(n,n')}\beta_{nn'}^i, \quad \text{(B2c)}$$

$$A_{nn,nn'}^i = \frac{\mu}{\sqrt{2}m_h\ell}\sqrt{\max(n,n')}\beta_{n'n}^i, \quad \text{(B2d)}$$

where $n'=n\pm1$; $i=x,y$; $\beta_{n,n\pm1}^x=\mp i$, and $\beta_{n,n\pm1}^y=1$. Using Eqs. (B2) in Eq. (12), we arrive at Eq. (13).

*Present address: Stanford Picosecond FEL Center, W. W. Hansen Experimental Physics Laboratory, Stanford University, Stanford, CA.

[1] See, e.g., C. A. Brau, *Free-Electron Lasers* (Academic Press, San Diego, 1990).

[2] For a review, see S. J. Allen, U. Bhattacharya, K. Campman, H. Drexler, A. Gossard, B. J. Keay, K. Maranowski, G. Medeiros-Ribeiro, M. Rodwell, J. S. Scott, C. Unterrainer, M. Wanke, and S. Zeuner, Physica B **227**, 367 (1996).

[3] B. J. Keay, S. J. Allen, Jr., J. Galán, J. P. Kaminski, K. L. Campman, A. C. Gossard, U. Bhattacharya, and M. J. W. Rodwell, Phys. Rev. Lett. **75**, 4098 (1995); B. J. Keay, S. Zeuner, S. J. Allen, Jr., K. D. Maranowski, A. C. Gossard, U. Bhattacharya, and M. J. W. Rodwell, *ibid.* **75**, 4102 (1995).

[4] H. Drexler, J. S. Scott, S. J. Allen, K. L. Campman, and A. C. Gossard, Appl. Phys. Lett. **67**, 2816 (1995).

[5] S. Zeuner, B. J. Keay, S. J. Allen, K. D. Maranowski, A. C. Gossard, U. Bhattacharya, and M. J. W. Rodwell, Phys. Rev. B **53**, R1717 (1996).

[6] K. Unterrainer, B. J. Keay, M. C. Wanke, S. J. Allen, D. Leonard, G. Medeiros-Ribeiro, U. Bhattacharya, and M. J. W. Rodwell, Phys. Rev. Lett. **76**, 2973 (1996).

[7] J. Kono, Y. Nakamura, X. G. Peralta, J. Černe, S. J. Allen, H. Akiyama, H. Sakaki, T. Sugihara, S. Sasa, and M. Inoue, Superlattices Microstruct. **20**, 383 (1996).

[8] N. Qureshi, J. S. Scott, S. J. Allen, Jr., M. Reddy, M. J. W. Rodwell, Y. Nakamura, I. Tanaka, T. Noda, I. Kamiya, and H. Sakaki, Physica B (to be published).

[9] J. Černe, J. Kono, M. S. Sherwin, M. Sundaram, A. C. Gossard, and G. E. W. Bauer, Phys. Rev. Lett. **77**, 1131 (1996).

[10] J. Černe, A. G. Markelz, M. S. Sherwin, S. J. Allen, M. Sundaram, A. C. Gossard, P. C. van Son, and D. Bimberg, Phys. Rev. B **51**, 5253 (1995).

[11] J. Kono, J. Černe, T. Inoshita, M. S. Sherwin, M. Sundaram, and A. C. Gossard, in *Proceedings of the 23rd International Conference on the Physics of Semiconductors*, edited by M. Scheffler and R. Zimmermann (World Scientific, Singapore, 1996), p. 1911.

[12] J. Kono, T. Inoshita, H. Sakaki, J. Černe, M. S. Sherwin, M. Sundaram, and A. C. Gossard, in *High Magnetic Fields in the Physics of Semiconductors II*, edited by G. Landwehr and W. Ossau (World Scientific, Singapore, 1997), p. 785.

[13] J. Černe, J. Kono, T. Inoshita, M. Sherwin, M. Sundaram, and A. C. Gossard, Appl. Phys. Lett. **70**, 3543 (1997).

[14] J. Kono, M. Y. Su, K. B. Nordstrom, J. Černe, M. S. Sherwin, S. J. Allen, Jr., T. Noda, T. Inoshita, and H. Sakaki, Proc. SPIE **3153**, 96 (1997).

[15] J. Kono, M. Y. Su, T. Inoshita, T. Noda, M. S. Sherwin, S. J. Allen, Jr., and H. Sakaki, Phys. Rev. Lett. **79**, 1758 (1997).

[16] Y. R. Shen, *The Principles of Nonlinear Optics* (Wiley, New York, 1984), Chap. 2.

[17] P. Y. Yu and M. Cardona, *Fundamentals of Semiconductors* (Springer-Verlag, Berlin, 1996), Sec. 9.2.

[18] P. Y. Yu and M. Cardona, *Fundamentals of Semiconductors* (Ref. 17), p. 69.

[19] G. Bastard, *Wave Mechanics Applied to Semiconductor Heterostructures* (Halsted Press, New York, 1988), Chap. 7.

[20] A. H. MacDonald and D. S. Ritchie, Phys. Rev. B **33**, 8336 (1986).

[21] G. E. W. Bauer and T. Ando, Phys. Rev. B **38**, 6015 (1988).

[22] H. Haug and S. W. Koch, *Quantum Theory of the Optical and Electronic Properties of Semiconductors*, 2nd ed. (World Scientific, Singapore, 1993), Chap. 19.

[23] M. L. Glasser and N. J. M. Horing, Phys. Rev. B **31**, 4603 (1985).